Using Field Asymmetric Ion Mobility Spectrometry for Odor Assessment of Automobile Interior Components

Juan Li, Ricardo Gutierrez-Osuna, *Senior Member, IEEE*, Ryan D. Hodges, Gail Luckey, Joel Crowell, Susan S. Schiffman, and H. Troy Nagle, *Life Fellow, IEEE*

***Abstract*— The of the quality of odors emitted from automobile cabin interiors is an important element for the design of vehicles that meet prospective customers' expectations. Extending our previous work on machine-versus-human odor assessment for intact automobile cabin interiors, in this paper, we evaluated odors generated from individual interior parts using a human panel and field asymmetric ion mobility spectrometry (FAIMS). We used image processing techniques to extract geometric features from FAIMS dispersion fields, and built the predictive models for three odor assessment parameters (intensity, irritation, and pleasantness) by means of partial least squares regression. The best feature set was chosen by backward sequential feature selection. Using *k*-fold cross validation, we achieved statistically significant correlation 0.95 between human panel measured and machine olfaction predicted odor assessment scores with a sample set of 48 interior automobile parts. These results, generated using the geometric image processing methods demonstrated herein, further support the feasibility of replacing a human panel by machine olfaction for the assessment of odor quality of interior automobile parts.**

***Index Terms*— Automobile odor assessment, field asymmetric ion mobility spectrometry, machine olfaction, image processing, partial least squares regression, k-fold cross-validation.**

I. INTRODUCTION

In ADDITION to reliability and safety, odor quality has become an important factor in customers' preferences when they acquire new automobiles. Odors inside automobiles are complex mixtures of volatile organic compounds (VOCs) that come in part from the materials of various interior parts. In order to improve customers' impressions of a manufacturer's automobile offerings, the odor (gas mixture) emitted from each part should be evaluated for its contribution to collective cabin odor. Conventionally, human panels are used to identify and evaluate odors. The interactions between the VOCs and the mammalian odor receptors create the human panelists' perceptions of the odor. However, because human panels are expensive and time-consuming [1], alternative sensor-based approaches are needed for detecting and identifying the odorous VOCs in a cost-effective and reliable way. Previously reported studies of automobile odors investigated the chemical compounds inside the cabin emitted by certain individual parts using gas chromatography-mass spectrometry (GC-MS), without addressing the accompanying odor quality attributes [2], [3].

Machine olfaction is a promising approach for this application. Traditional machine olfaction systems have been based on arrays of cross-selective sensors and pattern recognition methods, and have been called electronic noses (e-noses) [4]. Commonly employed cross-selective sensing technologies have included metal oxide semiconductor (MOS), MOS field effect transistor (MOSFET), conducting polymer (CP), surface and bulk acoustic wave (SAW, BAW), fluorescence (FL), infrared (IR) absorption, and photonics [5]. These sensing techniques have been employed in a wide range of application types with varying levels of success.

The odors inside automobile cabins for any specific manufacturer's model are generated by a wide range of different chemical compounds [2], so a very sensitive and broad chemical sensing technology is needed. In this work, we propose a machine olfaction system using a Lonestar field asymmetric ion mobility spectrometer (FAIMS) by Owlstone, Inc., and employ it to examine odors generated from different automobile parts. The Lonestar FAIMS generates two distinctive color images for each measurement test. In our case, we tested the odor of automobile interior materials before and after subjecting them to a company-specified heating cycle, a process that increased the available VOC concentrations. Changing VOC concentrations alters the shapes of features in the FAIMS-generated images. Since numerous VOCs emitted from automotive parts are known to occur in low concentrations [6], image processing methods that detect small changes in the image shapes were used to extract odor-relevant information from the acquired FAIMS spectral signals. Regression models based on selected features were built to predict standard odor sensory parameters for each automobile interior part. The models' performances were validated by *k*-fold cross-validation with the original professional human panel evaluation as a reference.

Manuscript received March 29, 2016; revised April 28, 2016; accepted April 29, 2016. Date of publication May 13, 2016; date of current version June 16, 2016. This is an expanded paper from the IEEE SENSORS 2015 Conference. The associate editor coordinating the review of this paper and approving it for publication was Dr. Richard T. Kouzes.

J. Li, R. D. Hodges, S. S. Schiffman, and H. T. Nagle are with North Carolina State University, Raleigh, NC 27695 USA (e-mail: jli35@ncsu.edu; rdhodges@ncsu.edu; sschiffman@nc.rr.com; nagle@ncsu.edu).

R. Gutierrez-Osuna is with Texas A&M University, College Station, TX 77840 USA (e-mail: rgutier@cse.tamu.edu).

G. Luckey and J. Crowell are with Hyundai Kia America Technical Center, Inc., Superior Township, MI 48198 USA (e-mail: gluckey@hatci.com; jcrowell@hatci.com).

Digital Object Identifier 10.1109/JSEN.2016.2568209

An early version of this work was presented at IEEE SENSORS 2015 [7]. This paper is organized as follows. Section II provides background of ion mobility spectrometry (IMS) and FAIMS. In Section III, we introduce related published literature on detection and identification of chemical compounds by IMS and FAIMS. Section IV describes the experimental setup and detailed procedures for data collection by our machine olfaction system. In Section V, we present the image-based feature extraction methods adapted for our FAIMS data, followed by a discussion of feature selection and model performance in Section VI. Finally, Section VII draws conclusions from our study.

II. BACKGROUND

Ion mobility spectrometry (IMS) is an alternative chemical characterizing technique to detect a wide variety of organic chemicals [8]. Developed for gas sensing in the early 1970s [8], [9], IMS has been used in prototype configurations for routine clinical, diagnostic measurements, and detection of chemical warfare agents, toxic industrial compounds, explosives and drugs of abuse [10]. Over the years, several types of ion mobility spectrometers have emerged. The term IMS is frequently associated with drift-time based systems, with other configurations being described as differential mobility spectrometers (DMS), travelling wave ion mobility spectrometers (TWIMS), and field asymmetric ion mobility spectrometers (FAIMS).

In this study, we employed a FAIMS device. FAIMS was introduced in the early 1990s. Its operation is based on the nonlinear behavior of ions in asymmetric electric fields [11]. Compared to traditional IMS, that injects ions into the drift region using an ion shutter and then separates ions by their mobility differences, FAIMS has no ion shutters and ions are continuously introduced into the analyzer. The asymmetric electric field, applied for nanoseconds with voltages up to 20,000 V/cm, accelerates the ion separation. These key differences improve the sensitivity and reduce the operational complexity. The commonly deployed ion sources for FAIMS are radioactive, corona discharge, photo discharge lamps, lasers and variations of ion electrosprays [8]. Many factors can affect the spectra, including the dispersive effects of diffusion and ion-ion repulsion [12], ion source saturation, as well as experimental parameters such as compensation voltage, temperature, moisture, pressure and sample impurities [13]. Unfortunately, no standard guidelines exist to optimize experimental conditions for ion mobility spectra. As such, finding odor-relevant information under different experimental conditions is the key challenge when using FAIMS for machine olfaction.

III. RELATED WORK

Low cost, portability, flexibility, sensitivity and selectivity make IMS an attractive technique for on-site, real time environmental monitoring and chemical detection. Tuovinen et al. [14] detected several pesticide compounds individually from liquid matrices using a six-electrode, flow-through type IMS model MGD-1. Three compounds (sulfotep, propoxur and nicotine) with 2-propanol as their solvent were tested at different concentrations. Based on the collected responses from six different IMS channels, a self-organizing map and Sammon's mapping methods provided by commercial Visual Nose software were used to find similarity between samples. The results show clear separation among the three pesticide compounds and their solvent.

A larger study of IMS detection of individual chemicals was carried out by Bell et al. [15]. They investigated the classification of 204 chemicals, each at various concentrations, from a standardized database of 3,137 IMS spectra. A two-tiered backpropagation neural network was proved to successfully detect 195 compounds represented by 1,293 spectra. A log transformation of acquired spectral data improved the performance of the neural network. They also found that features including drift times, peak numbers, peak intensity and peak shape were efficient for differentiating chemicals. A fixed feature combination was not capable of separating all classes of chemicals. Different feature combinations were needed for each class.

The determination of analytes in complex samples, or the mixtures of various target compounds, leads to complicated IMS signals. This may arise from multiple and competitive ionization interactions as a consequence of limited reactant ions in chemical-based sources or limited energy available in the ionization source. When a radioactive source is used, Márquez-Sillero et al. [16], noted that ionization of substances with low proton affinity is reduced when compounds with higher proton affinities are present. Similarly, in negative polarity, ionization of substances with higher electron affinities can hinder the ionization of analytes with lower electron affinities. Additionally, it is possible that different compounds having the same drift time are falsely identified as the same target analytes, leading to a false-positive response.

For gas mixtures, Snyder et al. [17] used a hand-held gas chromatography-ion mobility spectrometer (GC-IMS) combined with principal component analysis and discriminant analysis to separate compounds from three different types of gas mixtures. Gas mixture samples consisted of (1) fifteen compounds representative of illegal drug synthesis precursors/purification solvents; (2) eighteen compounds that are airborne contaminants in the NASA space shuttle; and (3) benzene, toluene, xylenes and six polyaromatic hydrocarbons among 41 alkane, alkene and alkylaromatic compounds typical of petroleum-based environmental contaminants. For dataset (1), principal component (PC) 1, 2 and 5 were capable of separating all types of compounds, which was similar to results by discriminant analysis. These three PCs accounted for about 76% of total variance in this dataset. In dataset (2), discriminant analysis provided clear separation of compounds, whereas principal components did not. For the third dataset, discriminant analysis identified more types of compounds than did principal components.

FAIMS has been employed in medical applications to differentiate patients during treatment. Covington et al. [18] used an electronic nose and FAIMS to analyze stool samples to detect patients at risk of gastrointestinal toxicity during pelvic radiotherapy. Fisher discriminant analysis of wavelet-transform processed FAIMS data showed the sample dataset was classified into four groups: low toxicity pre-treatment,

TABLE I
AUTOMOBILE PART SAMPLE IDENTIFIERS

Sample No.	Vehicle Model				
	A	B	C	D	E
a. Floor carpet	9	23	37	34	42
b. Floor mat	44	11	25	22	8
c. Headliner	45	24	26	1	43
d. Instrument panel	32	7	13	10	31
e. Rear package tray	33	12	14	none	none
f. Cloth bolster for seat cover	15	48	18	17	16
g. Cloth insert for seat cover	3	36	6	5	4
h. Leather bolster for seat cover	39	47	38	41	40
i. Leather insert for seat cover	27	35	30	29	28
j. Seat foam	21	19	2	46	20

high toxicity pre-treatment, low toxicity post-treatment, and high toxicity post-treatment.

In our previous study [19], we used FAIMS and photoionization detection to assess odors inside automobile cabins. Results showed a correlation (0.67-0.84) between model predictions and ground truth from a trained human panel. This study suggested that FAIMS can be used to predict odor sensory evaluations traditionally generated by a trained human panel.

As the above literature survey shows, prior work on IMS literature has focused on identifying and classifying VOC chemicals or biomarkers. While a handful of studies have explored the relationship between sensor signals and odor sensory quality evaluation [20]–[22], none with the exception of our prior work [19] have used FAIMS. So, we adopted the use of FAIMS in this application.

IV. EXPERIMENTS

In this project, North Carolina State University and Hyundai Motor Group partnered to explore the use of FAIMS in evaluating odors generated by heat-cycled interior cabin parts. Our goal was to develop signal processing algorithms to predict odor ratings of a trained human panel from FAIMS. In the experiments below, we describe our progress toward that goal.

A. Samples

Odor can emanate from a variety of parts comprising an automobile's interior cabin. Table I lists our selection of 10 types of parts (labeled from a to j) from five different automobile models (labeled from A to E). The selected parts were: floor carpet, floor mat, headliner, instrument panel, rear package tray, cloth bolster for seat cover, cloth insert for seat cover, leather bolster for seat cover, leather insert for seat cover, seat foam. Two of the models had no rear package tray, so a total of 48 samples were tested (each sample's identifying number is listed in Table I).

B. Human Panels

Our odor panel consisted of four trained evaluators. The detailed human panel training procedure can be found [19], [22]. During the experiments, each panel member sniffed each of the 48 samples and rated it for intensity, irritation, and pleasantness. For each evaluation parameter, panelists scored odors using a standard scale from 0 to 8, where a rating of 0 denotes no intensity, no irritation and extremely pleasant, and a rating of 8 means maximal odor intensity, maximal irritation and extremely unpleasant; neutral pleasantness is rated as four [23], [24].

C. Experimental Procedure

A four-liter glass jar was used as the sample container. The jar had a custom Teflon disc fashioned as a cover with two ports, one for extracting headspace odor samples and the other resupplying odorless clean dry air. Prior to each sample test, the jar's interior and exterior were cleaned using a standard company protocol using deionized water and ethyl alcohol (EtOH). This step removed odor residues left in the jar during previous tests. The clean empty jar was sealed and placed in a heated oven at 80°C for one hour. After removing the jar from oven, a SKC pump was used to transfer the headspace gas from jar to the FAIMS (Lonestar; Owlstone, Inc.) Three FAIMS measurements (each taking three minutes) were collected for the clean empty jar. These three measurements are used as background odor since in case some lingering residues survived our jar-cleaning process and introduced trace VOCs during the one-hour heating cycle.

Next, a representative piece from one of the 48 parts was placed inside the jar (typically cut in the shape of a small rectangular block $\approx$ 3"×4"×2"). The jar containing the sample piece was sealed and placed into an oven at 80°C for two hours. Following heating, the sealed jar with sample piece was removed from the oven and allowed to cool at room temperature for another hour. Then the four human panelists sniffed the odor from inside the jar by sliding the Teflon®cover slightly to the side, minimizing headspace dilution. Finally, the FAIMS measured the odor sample after human panelists finished their evaluation. For each sample piece, the FAIMS also acquired three measurements (each taking three minutes). This procedure was repeated for all 48 samples.

V. METHODS

To generate odor assessment parameters from FAIMS data, we extracted properties from the dispersion field matrix (DFM) images as described below. The goal was to build models generating highly correlated odor assessment predictions relative to ground truth human panel scores. Correlation coefficients higher than 0.95 were targeted. Before describing the signal processing algorithm, we summarize the specific parameters of the FAIMS unit used.

A. Lonestar Sample Data

The Lonestar FAIMS uses a flat-plate IMS technology in which ions move in a channel under strong electric field conditions. A Ni^{63} radiation source is employed to ionize the molecules in a pressurized air stream. This airstream transverses a conductive channel in which an alternating asymmetric electric

TABLE II

EXPERIMENTAL SETTINGS FOR LONESTAR FAIMS

Parameter	Value
Dispersion field	0%~100%
Compensation voltage	-6 V~ +6 V
Flow rate	1 L/min
Sensor temperature	60 °C
Pressure	-0.12 barg

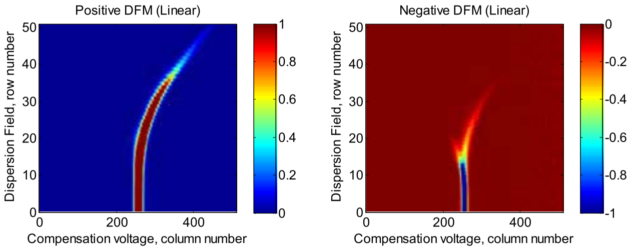

(a) (b)

Fig. 1. DFM of one floor mat sample piece. (a) Positive DFM. (b) Negative DFM.

field is applied along with a sweeping DC bias, which is swept as the amplitude of the alternating field is increased. Ions that reach the end of the channel (those that avoid colliding with the walls) generate a current proportional to the number of ions surviving the channel's electric field dynamics. A DFM for positive ions and negative ions respectively is the measured ion current as a function of applied DC bias and the amplitude of the applied asymmetric alternating electric field [25]. This leads to a unique identification for ions with the same mobility. The DC bias is swept from -6V to $+6$V in our experiments. All our parameter settings for the Lonestar are shown in Table II.

The positive and negative DFMs for one sample part are shown in Fig. 1. For different chemicals, the information shown in the positive and negative DFM may be different if they have different proton or electron affinity. In our measurements, each DFM has dimension 51×512. These data dimensions can be compared to a typical e-nose instrument that might generate data sets with dimension 16×30 (16 sensors sampled for 30 seconds) [21]. Therefore, finding a good feature extraction algorithm to reduce the FAIMS dataset to a limited number of highly related indicators of odor quality is even more important than for a typical e-nose instrument.

B. Image Features

As shown in Fig. 1, positive and negative DFMs can be plotted as images. Since the spectral profile is related to ion mobility, the shapes and positions of image features are determined by the specific chemicals in the gas mixture. We employed and compared 10 different feature subsets summarized in Table III, each containing 1 to 52,224 elements. We used MATLAB image-processing tools [26] to extract the feature elements as follows.

1) DFMs: For each odor sample, there is one 51×512 matrix for the positive DFM and one for the negative DFM. By considering each component in the matrix as one feature property, the matrix of positive and negative DF was transformed into 1-D $1 \times 26,112$ vector, respectively, then combining two 1-D vectors to form a 1-D $(1 \times 52,224)$ vector, which we denote as feature subset "DFMs".

TABLE III

SELECTED FEATURES FOR EACH ODOR SAMPLE

Feature Subset No.	Feature Subset Name	Dimension
1	DFMs	1×52224
2	Binary DFMs	1×52224
3	Total area of binary DFMs	1×1
4	Centroid	1×4
5	Boundary	1×52224
6	Perimeter of the boundary	1×1
7	Corner location	1×48
8	Bounding area parameters	1×10
9	Peak location and amplitude	1×110
10	Peak migration	1×4

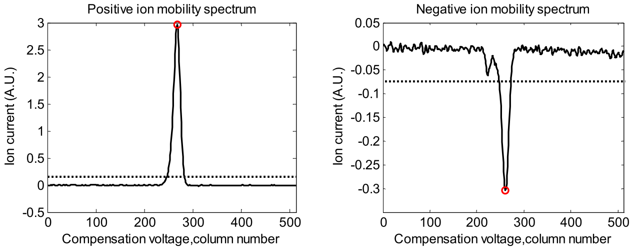

(a) (b)

Fig. 2. Ion mobility spectrum of one floor mat sample piece (DFM row 20). (a) Positive. (b) Negative.

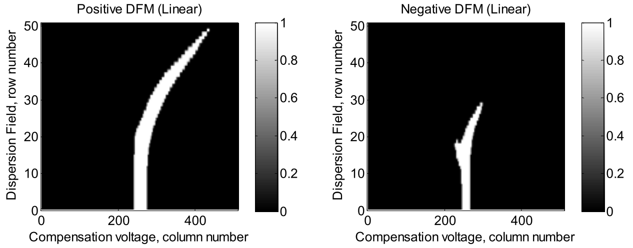

(a) (b)

Fig. 3. Binary DFMs. (a) Positive. (b) Negative.

2) Binary DFMs: Each row in a DFM is a spectral plot as shown in Fig. 2. In order to capture the spectral profile information of the DFM and remove noise signals, we turned the positive and negative DFMs into binary images by setting a threshold with absolute value 0.075 A.U. in Fig. 2. This process turns the DFMs into binary images (see Fig. 3), which we then process as done previously for the original DFMs to generate a 1-D $1 \times 52,224$ vector for each sample. Although the binary DFMs have same dimension as the original DFMs, the binary DFMs are sparser than the original DFMs (i.e., black pixels are set to zero); the main effect of binarization is to remove low-level noise.

3) Total Area of Binary DFMs: The total area of binary DFMs is the sum of non-zero (i.e., white) pixels in the binary DFM vector. Thus, this step generates a feature subset with one element.

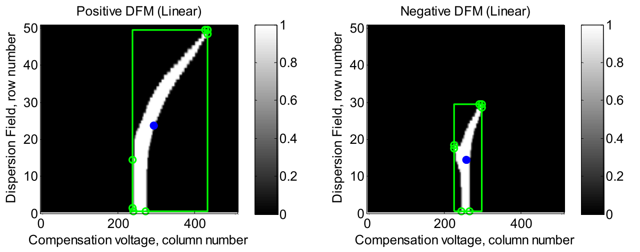

Fig. 4. Image features of DFM images of one floor mat sample piece. (a) Positive. (b) Negative. (Blue dot is centroid; green rectangle is bounding; green small circle is corner).

4) Centroid: The centroid is the center of the region of interest (over non-zero pixels), and can be derived as

$$C_x = \frac{1}{N}\sum_{i=1}^{N} x_i, \quad C_y = \frac{1}{N}\sum_{i=1}^{N} y_i \tag{1}$$

where (x_i, y_i) is the location of a white pixel and N is the total number of white pixels. The centroids of binarized DFM images can capture the spectral profile change among different odor samples. The centroids of the selected floor mat odor sample are shown as blue dots in Fig. 4. This feature subset contains four elements.

5) Boundary: The boundary of the DFM is detected using the Canny edge detection algorithm [27]. The Canny operator convolves the image with a symmetric 2-D Gaussian function and then differentiates the image along the normal to the edge direction. With the same standard deviation σ for both directions x and y, a 2-D Gaussian function can be defined as:

$$G = \exp(-\frac{x^2 + y^2}{2\sigma^2}) \tag{2}$$

The direction n is oriented normal to the direction of an edge to be detected:

$$n = \frac{\nabla(G * I)}{|\nabla(G * I)|} \tag{3}$$

where I is the image data and $*$ denotes convolution. An edge point is defined to be a local maximum of the image I along direction n after the operator G applied. Therefore, the edge can be calculated based on:

$$\frac{\partial^2}{\partial n^2} G * I = 0 \tag{4}$$

The boundary of DFM collected from the clean empty jar was also extracted. The common signal between the boundary from the clean empty jar DFM and the boundary from the odor sample DFM was subtracted from the boundary of sample DFM, removing signals generated by any possible odor contaminants that were missed in the cleaning process. Fig. 5 shows the boundary of one odor sample, the boundary of corresponding clean empty jar, and the boundary of odor sample after removing common signals. The processed boundary matrices including positive and negative DFM are also transformed into 1-D vector. This generates a feature subset with 52,224 elements.

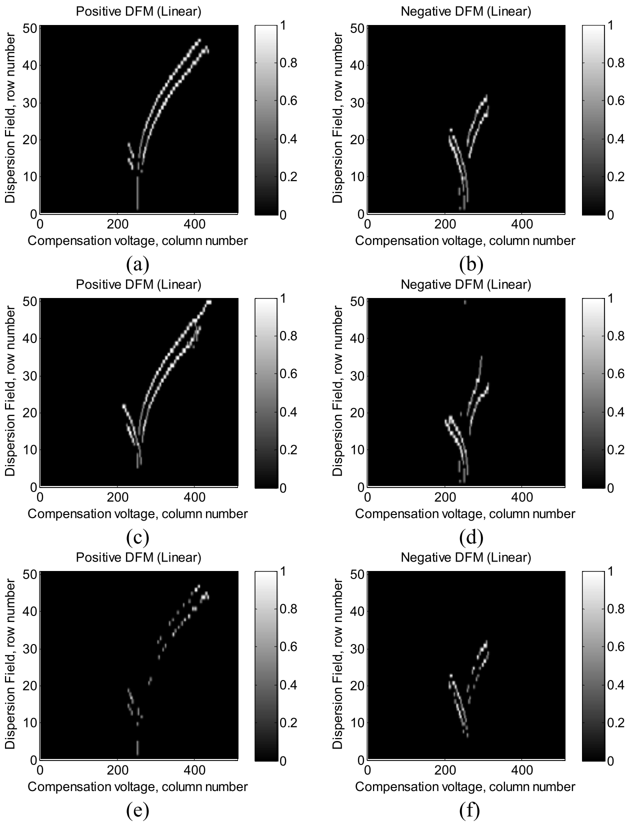

Fig. 5. Boundary. Odor sample: (a) Positive. (b) Negative. Clean empty jar: (c) Positive. (d) Negative. Odor sample after removing common signal: (e) Positive. (d) Negative.

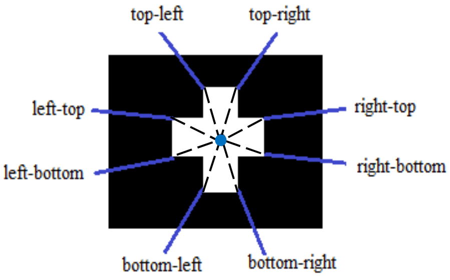

Fig. 6. Corner definition [26].

6) Perimeter of the Boundary: The perimeter of the boundary is calculated by summing the 1-D $1 \times 52,224$ boundary vector. As with the area feature subset, this process creates a feature subset with only one element.

7) Corner Location: The corner locations in each DFM binary image are capable of representing the tip location of branches, which is related to types of chemicals in the gas mixture. Consequently, an example of the eight corner positions of region of interest are chosen from the following points shown in Fig. 6: top-left, top-right, right-top, right-bottom, bottom-right, bottom-left, left-bottom, and left-top. The identified eight corner points in the selected sample are shown as small green circles in Fig. 4. In this feature subset, the locations of each identified corner on the *x,y* axes are extracted and ordered anti-clockwise from the bottom-left corner to left-bottom corner. This generates 16 elements for each of the two DFMs. In addition, the distance between each corner and the centroid of white region was also calculated (shown as black dash lines in Fig. 6) and ordered in the same as described above. This generates eight more elements for each of the two DFMs. Therefore, the corner location feature subset contains $16 \times 2 + 8 \times 2 = 48$ elements.

8) Bounding Area Parameters: This feature calculates the area of a rectangular box enclosing the region of interest. The rectangular box for the example sample is shown in green in Fig. 4. The location of the box area is defined by the x and y position of the box's lower-left corner. The area is computed as the product of the length and width of the box. The benefit of this method is to extract concurrently the region location, dimension ratio, and area. So, this feature subset includes five elements (the x and y position of the box's lower-left corner, the length and width of the box, and the area of the box) for each of the two DFMs, for a total of 10.

9) Peak Location and Amplitude: The peak locations are related to the types of positive or negative ions. Their amplitudes are correlated with the concentration of ions. The peak locations and amplitudes move around under different dispersion field conditions and can provide information highly related to characteristics of chemical components of the gas mixture. An example of detected peaks is shown in Fig. 2 as small red circles. The smaller peak in the negative DFM is a reactive ion peak related to the moisture level instead of the target chemicals, so it was not considered in our study. Based on spectral density of DFMs collected in our experiments, peak location and peak value were collected from rows 1 to 35 for the positive DFM and from rows 1 to 20 for the negative DFM, so the number of elements in the peak feature subset is $(35 + 20) \times 2 = 110$.

10) Peak Migration: Peak migration is defined as the change of location and value between the peak in the first row of DFM and the peak in the last selected row of DFM (row 35 for the positive DFM and row 20 for the negative DFM). This generates a feature subset with four elements for each sample.

C. Signal Processing

The variability of collected FAIMS data was calculated among three measurements of each sample for all 48 parts. Each measurement was represented by the Euclidean norm of its DFMs. To build regression models, both the "snapshot" principal component analysis (PCA) regression and the partial least squares (PLS) regression method were applied. By comparing the results from two regression methods, we were able to verify the feasibility of our methodology. In the PLS regression models, image features or feature subsets were used as independent variables instead of original FAIMS DFM data. The details and related results are introduced in next section.

VI. RESULTS AND DISCUSSION

Here will present our results in the following order. First, we demonstrate the stability of our data. Then we compare the two methods for analyzing the FAIMS data: 1) "snapshot" principal component analysis (PCA) and 2) geometric image feature extraction on FAIMS DFMs as described above. We found that geometric image feature extraction yields significantly better results.

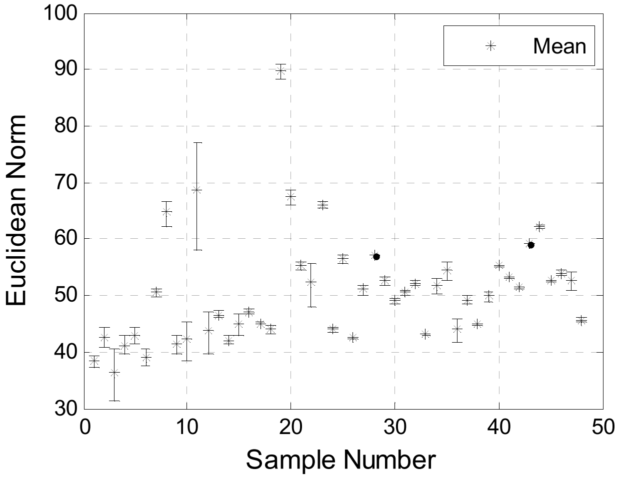

Fig. 7. Euclidean norm of measurements for each odor sample.

First, to ensure reliable measurements, the variability of our acquired Lonestar FAIMS data for each automotive part was tested by finding the Euclidean norm of three consecutive measurements. The positive and negative DFMs of each measurement were concatenated into a single 1-D vector with 52,224 elements, and then the Euclidean norm of each 1-D vector was calculated to represent each measurement. Differences among three consecutive measurements of all 48 samples are shown in Fig. 7 below.

In Fig. 7, the mean of Euclidean norm among three measurements for each of the 48 samples is marked by asterisk. The error bar shows the maximum and minimum norm value. The Euclidean norm $\tilde{x}_i$ of the ith measurement is calculated as:

$$\tilde{x}_i = \sqrt{\sum_{j=1}^{52224} x_{i,j}^2}, \quad i = 1, \cdots, m \tag{5}$$

where j is the jth dimension, and m is the total number of measurements ($3 \times 48 = 144$). The sample identification number is shown along the horizontal axis. All samples have deviation within 5% among their three measurements except Samples 3 and 11. Therefore, we used the arithmetic average of three measurements of each sample to reduce measurement noise.

A. Principal Component Analysis

Principal component analysis (PCA) is a commonly used e-nose feature extraction method. We used PCA on our FAIMS DFM data and then compared to the results of proposed image processing methods. In particular, we employed "snapshot" PCA [19], [28]. This method projects an average of three DFM measurements of each sample into independent directions based on their maximum variance matrix among

TABLE IV

CORRELATION BETWEEN LONESTAR MEASUREMENTS AND HUMAN PANEL DATA

Principal Components	Intensity	Irritation	Pleasantness
1	0.050	0.382	0.299
2	0.173	0.325	**0.403**
3	0.017	-0.041	0.073

TABLE V

CORRELATION BETWEEN PREDICTIONS AND ORIGINAL HUMAN PANEL DATA

No.	Feature Subset Name	Intensity	Irritation	Pleasantness
1	DFMs	0.275	0.431	0.441
2	Binary DFMs	0.433	0.516	**0.657**
3	Total area of binary DFMs	-0.048	0.418	0.422
4	Centroid	-0.192	0.409	0.436
5	Boundary	0.352	0.456	0.374
6	Perimeter of the boundary	-0.330	0.230	0.392
7	Corner location	0.330	0.527	0.418
8	Bounding area parameters	0.286	0.484	0.391
9	Peak location and amplitude	**0.534**	**0.611**	0.511
10	Peak migration	-0.313	0.364	-0.437

all 48 samples. The eigenvector for each direction is calculated by a linear combination of our averaged sample data; this avoids having to invert a large matrix. For our dataset, the first three out of 48 principal components (PCs) capture more than 90% of the variance and were used for all subsequent processing. The correlation between these three PCs and human panel evaluation scores is listed in Table IV.

Odor quality predictions, generated by principal component regression models based on these first three PCs, are correlated with human panel evaluation scores as -0.307 for intensity, 0.362 for irritation, and 0.287 for pleasantness after k-fold cross-validation ($k = 48$), with p-value are $p = 0.72$, $p < 0.01$, and $p < 0.01$, respectively. These correlation coefficient values are smaller than our goal 0.95, so we conclude that PCA is unable to extract highly relevant odor assessment information.

B. Partial Least Squares Regression Models Using Image Features

Partial least squares (PLS) can process collinear data and also reduce the number of required training samples [29]. Our previous study [19] shows that PLS works well for modeling and predicting odor sensory parameters for automobile cabin interiors. Therefore, in this study we also used PLS to build predictive models for corresponding automobile parts. PLS extracts "latent variables" from the directions of maximum correlation between dependent and independent variable matrices in a sequential fashion. In this study, the independent variables are image features extracted from FAIMS data and the dependent variables are human panel odor evaluation scores. Each latent variable is generated iteratively.

1) Models Using One Individual Feature Subset: The results of regression model using PLS method for each feature subset individually are shown in Table V. The regression model is verified by k-fold cross-validation ($k = 48$) in a leave-one-part-out fashion. The feature subset "Peak location and amplitude" generated the best regression models for intensity and irritation, whereas the feature "Binary DFMs" generated the best regression model for pleasantness. Although these results are better than those using PCA, these models using a single feature subset did not meet our performance goal.

TABLE VI

FEATURES SELECTED FOR INTENSITY

Feature No.	Feature Subset Name	Total Available Elements	Number of Selected Elements
6	Perimeter of the boundary	1	1
7	Corner location	48	17
8	Bounding area parameters	10	5
9	Peak location and amplitude	110	42
10	Peak migration	4	2

TABLE VII

FEATURES SELECTED FOR IRRITATION

Feature No.	Feature Subset Name	Total Available Elements	Number of Selected Elements
4	Centroid	4	2
6	Perimeter of the boundary	1	1
7	Corner location	48	20
8	Bounding area parameters	10	6
9	Peak location and amplitude	110	41

2) Sequential Feature Selection: In order to find the "optimal" subset that maximizes the predictive accuracy, sequential feature selection was employed. Sequential feature selection is a greedy search algorithm that finds a local optimum. It has two methods: forward selection and backward selection. Forward selection involves adding feature element sequentially from none to all. Conversely, backward selection is reducing feature element sequentially from all to none [4]. In our case, we put all the elements from the 10 feature subsets in Table III into one feature set with dimension $1 \times 156,850$. The model predictive accuracy was evaluated by k-fold cross-validation with $k = 48$. By examining the results of features selected from both the forward and backward methods, the backward selection method generated the highest correlation and predictive accuracy. The backward selected features for the PLS models are summarized in Tables VI, VII and VIII, for intensity, irritation and pleasantness, respectively. Feature subsets 1, 2, and 5 were not selected for any of the PLS models. A possible reason is that the dimension of these feature subsets is large and their represented information is included in other selected features. Feature subset 3 was also not selected for any model, which means the area of white pixels is not highly correlated with three human assessment parameters.

TABLE VIII

FEATURES SELECTED FOR PLEASANTNESS

Feature No.	Feature Subset Name	Total Available Elements	Number of Selected Elements
4	Centroid	4	2
6	Perimeter of the boundary	1	1
7	Corner location	48	20
8	Bounding area parameters	10	4
9	Peak location and amplitude	110	42
10	Peak migration	4	2

TABLE IX

MODEL ACCURACY

Parameter	Number of Latent Variables	Correlation	p-value	RMS
Intensity	15	0.951	<0.01	0.224
Irritation	12	0.951	<0.01	0.258
Pleasantness	28	0.950	<0.01	0.172

For the selected feature subsets 4, and 7-10, some of their elements were not selected. For example, for the PLS model for odor intensity, $1+48+10+110+4 = 173$ total elements were available from feature subsets 6-10, respectively, but only $1 + 17 + 5 + 42 + 2 = 67$ of these elements were used in the model. For the PLS model for odor irritation, only 70 of 173 elements of the five selected feature subsets were needed. Finally for the PLS model for pleasantness, only 71 of 177 elements of the six selected feature subsets were needed.

Table IX illustrates the performance of our PLS model for each odor parameter based on the feature subsets in Tables VI, VII, and VIII. In order to reach our goal of 0.95 correlation between the human panel and our PLS models, the latent variables were allowed to increase as needed. This resulted in one set of 28 latent variables, slightly higher than half of our 48 samples. Using k-fold cross-validation ($k = 48$), the root mean square (RMS) error of model predictions of testing samples is also listed in Table IX. The RMS of all the three models is smaller than 0.26 units. Note that the odor parameter range is from 0 to 8. Therefore, it can be concluded that one may use a PLS regression model independently for each human assessment parameter, and that those models are capable of providing suitable predictions of odor intensity, irritation and pleasantness.

3) Learning Curve of Regression Models: In order to investigate the models' general performance, the learning curves for the three models were generated by employing testing sample sizes of 24, 16, 12, 8, 6, 4, 3, 2 and 1, and their related training sample sizes of 24, 32, 36, 40, 42, 44, 45, 46 and 47. The testing samples were selected based on k-fold cross-validation. The selected number of training and testing samples covered all the possible choices of k with our total sample size being 48. The training error and testing error were calculated based on RMS. The correlation between the three PLS models and the human panel, the training error, and the testing error are shown in Fig. 8. Note that the correlation results are above 0.90 for training sets greater than or equal 42.

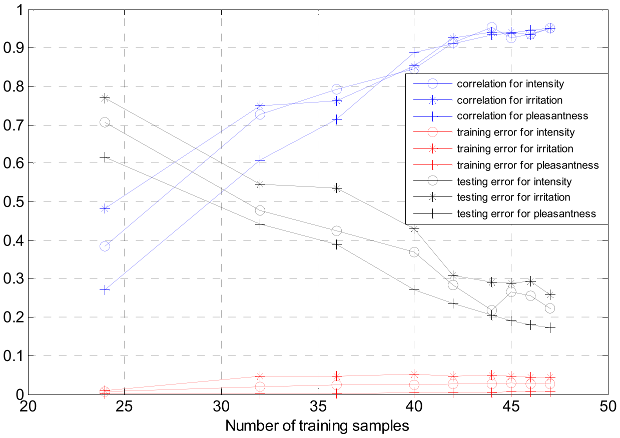

Fig. 8. Learning curve for three best regression models.

TABLE X

RATING STATISTICS OF HUMAN PANELISTS

Parameter	Standard Deviation			RMS Error Range of Machine Predictions
	Minimum	Median	Maximum	
Intensity	0.43	0.83	1.79	0.22-0.71
Irritation	0.43	0.83	1.79	0.26-0.78
Pleasantness	0	0.71	1.66	0.17-0.62

The testing error for three parameters is 0.26 units or smaller for the same training sets, and is decreasing and approaching the training error curve with increasing number of training samples. Ideally, the difference between the testing error and the training error should be less than the training error. Our curves are trending towards that goal, indicating that there was no overfitting in the three models and that a larger sample size should improve model performance.

The rating statistics of the human panelists for all 48 samples is presented in Table X. As explained above, four trained panelists were employed to evaluate each sample on three criteria (intensity, irritation, and pleasantness) within a scaling range from 0 to 8. The standard deviations among the four panelists' scores were calculated. The minimum value, median value, and maximum value for each parameter are shown in Table X. The entries compare the machine predictions' RMS error range with the human panel's standard deviations. The machine predictions' RMS errors have smaller values. Therefore, our sensor-based machine olfaction system generates results with less variability than the human panel.

VII. CONCLUSIONS

This study showed that geometric image processing of FAIMS data is a feasible method for replacing a human panel for the assessment of odor quality of automobile component parts within the vehicle's cabin. This paper is an extension of our previous work that demonstrated a FAIMS-based system was able to predict human odor assessments of automobile interior cabin environments [19]. Use of electronic systems to evaluate odor quality of vehicle parts and cabins will reduce human exposure to unpleasant mixtures of VOCs, some of which have exposure limits due to their toxicity. Odors generated by interior parts must not be regarded as offensive by prospective buyers of new automobiles. Identifying an offensive odor source from multiple vehicle parts and evaluating human olfactory preference for those parts are essential steps in the testing process. Herein, we have designed a system to mimic a human panel's ability to perform these tests and generate odor rating parameters in a reliable way.

To the best of our knowledge, we report in this project the first application of image processing techniques to extract features, and identify appropriate feature subsets, from FAIMS measurements. The PLS regression method builds three predictive models estimating three human odor sensory rating parameters of the target parts. Specific feature subsets were chosen independently for intensity, irritation and pleasantness. The regression model for each parameter generated by its selected feature subsets can reach a correlation with human panel scores higher than 0.95 with p-value smaller than 0.01. The RMS error of the three models for testing samples is smaller than 0.26 units on the 9-point odor scales. Even though the learning curve in Fig. 8 did not completely converge with our sample set totaling 48, it demonstrates that our regression modeling method for the three odor parameters is applicable, and should prove consistent and accurate when a larger sample set is available.

In conclusion, machine olfaction based on FAIMS and geometric image feature extraction has proven feasible as a human-panel replacement to provide sensory ratings on odor intensity, irritation and pleasantness for automobile interior components.

REFERENCES

[1] M. Morvan, T. Talou, and J.-F. Beziau, "MOS–MOSFET gas sensors array measurements versus sensory and chemical characterisation of VOC's emissions from car seat foams," *Sens. Actuators B, Chem.*, vol. 95, nos. 1–3, pp. 212–223, 2003.

[2] T. Yoshida and I. Matsunaga, "A case study on identification of airborne organic compounds and time courses of their concentrations in the cabin of a new car for private use," *Environ. Int.*, vol. 32, no. 1, pp. 58–79, 2006.

[3] E.-L. Kalman, A. Löfvendahl, F. Winquist, and I. Lundström, "Classification of complex gas mixtures from automotive leather using an electronic nose," *Anal. Chim. Acta*, vol. 403, nos. 1–2, pp. 31–38, 2000.

[4] R. Gutierrez-Osuna, "Pattern analysis for machine olfaction: A review," *IEEE Sensors J.*, vol. 2, no. 3, pp. 189–202, Jun. 2002.

[5] A. D. Wilson and M. Baietto, "Applications and advances in electronic-nose technologies," *Sensors*, vol. 9, no. 7, pp. 5099–5148, Jan. 2009.

[6] T. Yoshida, I. Matsunaga, K. Tomioka, and S. Kumagai, "Interior air pollution in automotive cabins by volatile organic compounds diffusing from interior materials: I. Survey of 101 types of Japanese domestically produced cars for private use," *Indoor Built Environ.*, vol. 15, no. 5, pp. 425–444, 2006.

[7] J. Li *et al.*, "Odor assessment of automobile interior components using ion mobility spectrometry," in *Proc. IEEE Sensors*, Busan, South Korea, Nov. 2015, pp. 1–4.

[8] G. A. Eiceman, Z. Karpas, and H. H. Hill, Jr., *Ion Mobility Spectrometry*, 3rd ed. Boca Raton, FL, USA: CRC Press, 2013, pp. 24–29 and 71.

[9] W. Baether, S. Zimmermann, and F. Gunzer, "Pulsed ion mobility spectrometer for the detection of toluene 2, 4-diisocyanate in ambient air," *IEEE Sensors J.*, vol. 12, no. 6, pp. 1748–1754, Jun. 2012.

[10] H. Borsdorf, T. Mayer, M. Zarejousheghani, and G. A. Eiceman, "Recent developments in ion mobility spectrometry," *Appl. Spectrosc. Rev.*, vol. 46, no. 6, pp. 472–521, 2011.

[11] I. A. Buryakov, E. V. Krylov, E. G. Nazarov, and U. Kh. Rasulev, "A new method of separation of multi-atomic ions by mobility at atmospheric pressure using a high-frequency amplitude-asymmetric strong electric field," *Int. J. Mass Spectrometry Ion Process.*, vol. 128, no. 3, pp. 143–148, 1993.

[12] R. Guevremont, "High-field asymmetric waveform ion mobility spectrometry: A new tool for mass spectrometry," *J. Chromatograph. A*, vol. 1058, nos. 1–2, pp. 3–19, 2004.

[13] R. A. Miller, G. A. Eiceman, E. G. Nazarov, and A. T. King, "A novel micromachined high-field asymmetric waveform-ion mobility spectrometer," *Sens. Actuators B, Chem.*, vol. 67, no. 3, pp. 300–306, 2000.

[14] K. Tuovinen, M. Kolehmainen, and H. Paakkanen, "Determination and identification of pesticides from liquid matrices using ion mobility spectrometry," *Anal. Chim. Acta*, vol. 429, no. 2, pp. 257–268, 2001.

[15] S. Bell, E. Nazarov, Y. F. Wang, and G. A. Eiceman, "Classification of ion mobility spectra by functional groups using neural networks," *Anal. Chim. Acta*, vol. 394, nos. 2–3, pp. 121–133, 1999.

[16] I. Márquez-Sillero, E. Aguilera-Herrador, S. Cárdenas, and M. Valcárcel, "Ion-mobility spectrometry for environmental analysis," *TrAC Trends Anal. Chem.*, vol. 30, no. 5, pp. 677–690, 2011.

[17] A. P. Snyder, W. M. Maswadeh, G. A. Eiceman, Y.-F. Wang, and S. E. Bell, "Multivariate statistical analysis characterization of application-based ion mobility spectra," *Anal. Chim. Acta*, vol. 316, no. 1, pp. 1–14, 1995.

[18] J. A. Covington *et al.*, "The detection of patients at risk of gastrointestinal toxicity during pelvic radiotherapy by electronic nose and FAIMS: A pilot study," *Sensors*, vol. 12, no. 10, pp. 13002–13018, 2012.

[19] J. Li *et al.*, "Odor assessment of automobile cabin air with field asymmetric ion mobility spectrometry and photoionization detection," *IEEE Sensors J.*, vol. 16, no. 2, pp. 409–417, Jan. 2016.

[20] S. S. Schiffman, R. Gutierrez-Osuna, and H. T. Nagle, "Measuring odor intensity with E-noses and other sensor types," in *Proc. 9th Int. Symp. Olfaction Electron. Nose*, Rome, Italy, Sep./Oct. 2002, pp. 68–72.

[21] R. Gutierrez-Osuna, S. S. Schiffman, and H. T. Nagle, "Correlation of sensory analysis with electronic nose data for swine odor remediation assesment," in *Proc. 3rd Eur. Congr. Odours, Metrology Electron. Noses*, Paris, France, Jun. 2001, pp. 1–5.

[22] T. C. Pearce, S. S. Schiffman, H. T. Nagle, and J. W. Gardner, *Handbook of Machine Olfaction: Electronic Nose Technology*. Darmstadt, Germany: Wiley, 2006.

[23] S. S. Schiffman, B. G. Graham, and C. M. Williams, "Dispersion modeling to compare alternative technologies for odor remediation at swine facilities," *J. Air Waste Manage. Assoc.*, vol. 58, no. 9, pp. 1166–1176, 2008.

[24] S. S. Schiffman, C. E. Studwell, L. R. Landerman, K. Berman, and J. S. Sundy, "Symptomatic effects of exposure to diluted air sampled from a swine confinement atmosphere on healthy human subjects," *Environ. Health Perspect.*, vol. 113, no. 5, pp. 567–576, 2005.

[25] *Lonestar Ion Mobility Spectrometer*, accessed on Jul. 2013. [Online]. Available: http://support.owlstonenanotech.com/entries/21639817-Introduction-to-FAIMS

[26] *MATLAB Image Processing Toolbox*, accessed on Jun. 2014. [Online]. Available: http://www.mathworks.com/help/images/ref/regionprops.html#bqkf8iq

[27] J. Canny, "A computational approach to edge detection," *IEEE Trans. Pattern Anal. Mach. Intell.*, vol. PAMI-8, no. 6, pp. 679–698, Nov. 1986.

[28] L. Sirovich, "Turbulence and the dynamics of coherent structures. I—Coherent structures. II—Symmetries and transformations. III—Dynamics and scaling," *Quart. Appl. Math.*, vol. 45, pp. 561–571, Oct. 1987.

[29] P. Geladi and B. R. Kowalski, "Partial least-squares regression: A tutorial," *Anal. Chim. Acta*, vol. 185, pp. 1–17, Nov. 1986.

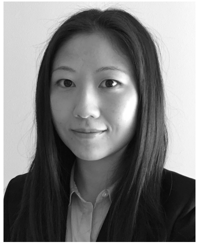

Juan Li received the B.S. degree in electrical engineering from Sichuan University, Chengdu, China, in 2006, and the M.S. degree in electrical engineering from the Beijing University of Aeronautics and Astronautics, Beijing, China, in 2009, and the Ph.D. degree in electrical engineering from North Carolina State University, Raleigh, in 2015. Her research interests include machine olfaction, signal processing, pattern recognition, and machine learning.

Ricardo Gutierrez-Osuna (M'00–SM'08) received the B.S. degree in electrical engineering from the Polytechnic University of Madrid, Madrid, Spain, in 1992, and the M.S. and Ph.D. degrees in computer engineering from North Carolina State University, Raleigh, in 1995 and 1998, respectively. From 1998 to 2002, he served as a Faculty Member with Wright State University. He is currently a Professor of Computer Engineering with Texas A&M University. His research interests include pattern recognition, neuromorphic computation, chemical sensor arrays, and audio-visual speech processing.

Ryan D. Hodges received the B.S. and Ph.D. degrees in electrical engineering from North Carolina State University, in 2007 and 2014, respectively. He is currently a Post-Doctoral Research Scholar with North Carolina State University. He is currently involved in research with the ASSIST Center, a NSF Engineering Research Center geared towards the development of self-powered medical devices based on ultra-low power electronics and on-body energy harvesting.

Gail Luckey received the B.A. degree in business from William Tyndale College, and the B.S. degree in textile technology and the M.S. degree in textiles engineering and statistics from North Carolina State University, in 1978 and 1986, respectively. In 1986, she accepted an engineering position with General Motors (Inland Fisher Guide Division), where she was involved in various engineering capacities, manufacturing planning and marketing as a Cross-Brand Manager for Chevrolet. She joined the Hyundai-Kia America Technical Center, Inc., in vehicle development in 2002. She is currently with the Materials Development focusing on interior soft trim materials and in-cabin air quality. She is a member for the SAE VOC Committee.

Joel Crowell is currently a Chief Research Technician with the Materials Department, Hyundai-Kia America Technical Center Inc., where he is responsible for all polymer, textiles, and foam testing of automotive materials. He has been with industry for over 20 years, 10 years with HATCI and over 11 years with BASF Corporation, focusing on polymers and urethanes.

Susan S. Schiffman is currently an Adjunct Professor of Electrical and Computer Engineering with North Carolina State University. She has authored over 300 articles on the topic of smell and taste that span the range from clinical to molecular investigations. The findings of her research have appeared in many journals including *The New England Journal of Medicine*, *Proceedings of the National Academy of Sciences*, and the *Journal of the American Medical Association*. She is the co-editor of *Handbook of Machine Olfaction*. Her current research is focused on the development of instrumentation and sensors for environmental monitoring including electronic noses.

H. Troy Nagle (S'62–F'83–LF'08) received the B.S.E.E. and M.S.E.E. degrees from the University of Alabama, the Ph.D. degree in electrical engineering from Auburn University, and the M.D. degree from the School of Medicine, University of Miami. He is co-founder of Premitec, Inc., a medical device company based on technologies developed at NC State University. He is a registered professional engineer. He is currently a Distinguished Professor of Electrical and Computer Engineering with North Carolina State University (NCSU), and a Professor of Biomedical Engineering with UNC and NCSU. He was the Founding Chair of the UNC-NCSU Joint Department of Biomedical Engineering from 2003 to 2009. He has widely published in data acquisition and signal processing, and co-authored textbooks in digital logic design and digital control systems, and co-edited a handbook on *machine olfaction*. In recent years, he has focused his research on machine olfaction and experimented with its use in food processing, environmental monitoring, and medical diagnostics. He is a Fellow of the American Institute for Medical and Biological Engineering. He served as the IEEE President in 1994. He also served as an Editor-in-Chief of the IEEE SENSORS JOURNAL from 2003 to 2009. He is the Past President of the IEEE Sensors Council.